ELEVENTH EUROPEAN ROTORCRAFT FORUM

Paper No. 73

PREDICTION OF BLADE STRESSES
DUE TO GUST LOADING

Gunjit Singh Bir
Graduate Student

and

Inderjit Chopra
Associate Professor

September 10-13, 1985
London, England

Center for Rotorcraft Education and Research
Department of Aerospace Engineering
University of Maryland
College Park, Maryland 20742, USA

PREDICTION OF BLADE STRESSES DUE TO GUST LOADING

Gunjit Bir, Graduate Student
and
Inderjit Chopra, Associate Professor

Center for Rotorcraft Education and Research, Department of Aerospace Engineering
University of Maryland, College Park, MD 20742, USA

ABSTRACT

An analysis is developed for investigating the response of a rotor-fuselage system in a three-dimensional gust field wherein the gust velocity components can have arbitrary variation in space and time. Each rotor blade undergoes flap bending, lag bending and torsional deflections. The blades are divided into beam elements and each element consists of fifteen nodal degrees of freedom. Quasisteady strip theory is used to obtain the aerodynamic loads. Unsteady aerodynamic effects are introduced through dynamic inflow modelling. Dynamic stall and reverse flow effects are also included. The fuselage is allowed five degrees of freedom: vertical, longitudinal, lateral, pitch and roll motions. The gust response equations are linearized about the vehicle trim state and the blade steady-state deflected position, and then solved by time integration. The blade bending moments, which determine blade stresses, are evaluated using the force summation technique. Systematic studies are made to identify the importance of several parameters including dynamic stall, forward speed, lag stiffness, gust profile gust penetration rate and gust velocity direction.

NOTATIONS

a = blade lift curve slope
c = blade chord
C_d = blade section drag coefficient
C_ℓ = blade section lift coefficient
$C_{m_{ac}}$ = blade section moment coefficient about the aerodynamic center
$[C]$ = damping matrix in response equations
C_T = thrust coefficient, $T/\pi\rho\Omega^2R^4$
C_{m_x}, C_{m_y} = rolling and pitching moment coefficients
e_d = aerodynamic center offset from elastic axis, positive aft
f = equivalent flat-plate drag area of helicopter
$\bar{F}$ = resultant rotor force vector
$\vec{F}_h$ = hub-motion induced inertia force vector acting at a point (ξ,η) in the blade section
h = vertical distance of hub center from the helicopter c.g.
$\bar{I}$ = unit vector
I_{x_1}, I_{y_1}, I_{z_1} = helicopter roll, pitch and yaw moments of inertia about the hub center
$I_{x_1y_1}, I_{y_1z_1}, I_{z_1x_1}$ = helicopter products of inertia
m = mass per unit length of blade
m_o = reference mass per unit length
M = mass of the helicopter
$[M]$ = mass matrix in response equations
M_ϕ = aerodynamic moment per unit length about elastic axis
n = blade number
N = number of elements
N_b = number of blades
q = nodal displacement
$\bar{Q}$ = moment vector
R = rotor radius
t = time
T_1, T_2, T_3 = coordinate transformation matrices
u, v, w = elastic displacements in x,y,z directions, respecitvely
U_G, V_G, W_G = gust velocity components at a blade section
$\underset{\sim}{U}_G$ = column vector of gust velocities
U_R, U_T, U_P = air velocity components relative to a blade section in the negative ξ,η,ζ directions, respectively
U_x, U_y, U_z = air velocity components relative to a blade section in the x,y,z directions, respectively
V = helicopter forward velocity
$\bar{V}$ = wind velocity vector at a blade section

$[K]$ = stiffness matrix in response equations

k_x, k_y = *constants in Dree's inflow* model

$\underset{\sim}{\ell}$, $\underset{\sim}{m}$ = coefficient matrices in the dynamic inflow equations

L_u, L_v, L_w = blade aerodynamic forces per unit length in u, v, w directions, respectively

$\bar{L}_u$, $\bar{L}_v$, $\bar{L}_w$ = blade aerodynamic forces per unit length in ξ, η, ζ directions, respectively

$\bar{x}$, $\bar{y}$, $\bar{z}$ = inertial frame coordinates

X_H, Y_H, Z_H = hub-fixed coordinates

x_h, y_h, z_h = displacements of the perturbed hub center wrt the the unperturbed hub-fixed system

x_1, y_1, z_1 = unperturbed-hub-fixed coordinates

x_2, y_2, z_2 = perturbed-hub-fixed coordinates

α = blade section angle of attack

α_d = delayed angle of attack

α_{ds} = dynamic stall angle

α_{re} = flow reattachment angle

α_{max} = maxium allowable delay *angle*

α_s^o = steady shaft tilt, positive forward

α_s = perturbation shaft tilt, positive forward

α_T = total shaft tilt, positive forward

β_p = blade precone angle

γ = blade Lock number

ϵ = a small quantity, typically representing deformed elastic axis

$\delta(\ )$ = virtual variation

δT, δU = variations of kinetic and strain energies, respectively

δW = virtual work done by aerodynamic *and hub motion induced* inertia loads

Δ = perturbation

λ = rotor inflow ratio

$\bar{V}_b$ = blade velocity relative to hub-fixed coordinates

$\bar{V}_i$ = *induced* flow at a blade section normal to the hub plane

$\bar{V}_G$ = gust velocity vector at a blade section

$\bar{V}_h$ = hub velocity vector wrt the inertial frame

x, y, z = rotating undeformed blade coordinates

x_{ac} = distance of aerodynamic center from leading edge

Λ = yawed flow angle

λ_o, λ_{1s}, λ_{1c} = rotor inflow variables

μ = advance ratio, $V \cos\alpha_s^o/\Omega R$

ξ, η, ζ = deformed blade coordinates

ρ = air density

ρ_s = structural density

σ = solidity ratio $N_b c/\pi R$

ϕ = elastic twist about the elastic axis

$\hat{\phi}$ = geometric twist

ϕ_s^o = steady lateral tilt of the shaft, positive to the right

ψ_o = azimuth angle of the reference blade (No. 1) at time $\psi = 0$

ψ = *nondimensionalized time*, Ωt

ψ_n = azimuth position of blade n at time ψ

τ_L, τ_D, τ_M = delay time constants in the dynamic stall model

$\bar{\omega}_h$ = fuselage angular velocity vector

θ_{FP} = climb angle in steady flight

Ω = rotor rotational speed

Subscripts and Superscripts

H	: related to hub motion
A	: related to aerodynamic force
$(\dot{\ })$	: $\partial/\partial t(\ )$
C	: circulatory
NC	: noncirculatory
~	: *matrix*
{ }	: column vector
—	: vector quantity
o	: steady-state value

INTRODUCTION

Hingeless rotors have been gaining growing acceptance from industry because of mechanical simplicity, improved maintainability and higher control power. However, hingeless rotors experience large dynamic stresses, large hub loads and are susceptible to many other dynamic problems. One concern is the response of a hingeless rotor in a gusty environment. Gust-induced response influences the fatigue life of the structural components, vehicle controllability and ride quality. An understanding of dynamic stresses caused by gust loading would help in improving the rotor design.

The objective of the present study is to predict blade stresses and hub loads experienced by hingeless *rotors exposed to different* types of gust inputs.

Gust response of a helicopter is a complex aeroelastic phenomenon involving blade and hub motions, and only selected attempts have been made to investigate this problem. Arcidiacono et al[1] analytically studied the response characteristics of a helicopter subjected to vertical gusts. The analysis included the effects of dynamic stall, but the inflow was assumed to be steady during the gust induced loading. Azume and Saito[2] used local momentum theory to investigate the gust response of a model rotor and correlated the theoretical results with the wind tunnel results. The anlaysis considered a flap-bending blade subjected to vertical gusts only. Yasue et al[3] studied the gust response of a hingeless blade and correlated the analytical results with the wind tunnel results. Johnson[4] made an extensive gust response analysis of tilt-rotor aircrafts under crusiing flight conditions. Recently, the present authors[5] developed a general formulation to study the transient response of a coupled rotor-fuselage system exposed to a three-dimensional gust field. Dynamic inflow was included. Each blade was assumed to undergo flap bending, lag bending and torsion deflections. Response of hingeless rotor was calculated for several types of gust inputs. The other papers relevant to this topic are Refs. 6 - 8.

In all these papers[1-8], the emphasis is on the general gust response of rotor and fuselage systems. There is only a limited reference to the determination of gust-induced blade stresses and hub loads which is the scope of the present paper. The analysis adopted here is an extension of the previous work[5] through inclusion of dynamic stall and reversed flow effects.

Finite element formulation based on Hamilton's principle is used to examine the transient gust response of a rotor-fuselage system in forward flight. The blade is idealized as an elastic beam and is divided into a number of beam elements. Each element has five nodes and fifteen nodal degrees of freedom. The formulation is applicable to a nonuniform blade having pretwist, precone, and chordwise offsets of the center of mass, aerodynamic center and tension center from the elastic axis. The fuselage is modelled as a rigid body with three translational and two rotational degrees of freedom. The aerodynamic loads are obtained using quasisteady strip theory. Noncirculatory aerodynamic forces are also included. For steady inflow calculations a linear variation of inflow (Drees' model) is used. For unsteady induced flow calculations a dynamic inflow model[9] is used. Dynamic stall and reversed flow effects are included, but compressibility effects are ignored in the present analysis. The gust response solution is obtained in three phases. First, the vehicle trim solution is determined from the nonlinear equilibrium equations; the propulsive trim gives the rotor control settings and the vehicle orientation for a prescribed flight condition. The second phase involves the determination of the azimuth-dependent blade equilibrium position. The Floquet theory is used to solve the blade nonlinear periodic equations iteratively. In the final phase, equations governing the coupled rotor-fuselage dynamics are linearized about the vehicle trim and blade equilibrium positions. To reduce computation time, the equations in terms of nodal displacements are transformed into modal space using the rotating blade natural vibration characteristics. The response equations are solved by a time integration technique. Force summation method is then applied to calculate the blade dynamic stresses.

The effect of several parameters on the helicopter transient response is examined, including dynamic inflow, dynamic stall, lag stiffness, forward speed, gust profile, gust penetration speed and gust velocity direction.

FORMULATION

The general formulation and analysis details are given in Refs. 5 and 10-12 and are therefore briefly treated here. The helicopter is modelled as a rigid fuselage with N_b elastic blades. Each blade undergoes flap bending, lag bending, and torsion deflections. Fuselage motion participates in the blade equations of motion since it influences the blade aerodynamic and inertia loads. Similarly, the influence of blade motion is considered in the derivation of the fuselage equilibrium equations.

Figures 1(a)and 1(b) show respectively the unperturbed and gust-perturbed positions of the helicopter. The coordinate system (x,y,z) represents the inertial frame, (x_1,y_1,z_1) represents unperturbed hub-fixed reference frame, (x_2,y_2,z_2) represents the perturbed hub-fixed frame, and (x,y,z) denotes the blade-fixed rotating frame. α_T and ϕ_T are the tilts of the hub plane about the y_2-axis and the x_2-axis respectively. The body tilt angles α_T and ϕ_T are assumed to be of the order of $\varepsilon^{3/2}$, where ε represents typical elastic bending slope.

Blade Equations of Motion

Deformed positions of the blade, both in the steady-state and gust-disturbed flight conditions, are shown in Fig. 2. The azimuth position of the n^{th} blade is

$$\psi_n = \psi_0 + 2\pi(n-1)/N_b \tag{1}$$

where ψ_0 is the azimuth position of the reference blade (blade 1) at time $\psi = 0$. The x-axis coincides with the undeformed elastic axis. The degrees of freedom are the axial deflection u, the lag deflection v, the flap deflection w, and the twist $\hat{\phi}$ given by

$$\hat{\phi} = \phi - \int_0^r v''w'\, dr \tag{2}$$

where ϕ is the elastic twist of a section about the deformed elastic axis and $\hat{\phi}$ is the geometric twist about the undeformed elastic axis.

The formulation is based on Hamilton's principle

$$\int_{t_1}^{t_2} (\delta U - \delta T - \delta W)dt = 0 \tag{3}$$

where δU, δT, δW are respectively the variations in the strain energy, the kinetic energy and the virtual work done by the external forces. The expressions for δU and δT are given in Ref. 12 and the expression for δW is

$$\delta W = \int_0^R (L_u \ \delta u + L_v \ \delta v + L_w \ \delta w + M_\phi \ \delta\psi)dx \tag{4}$$

where L_u, L_v, L_w and M_ϕ represent the combined aerodynamic and hub-motion induced inertia forces distributed along the blade length in the axial, lead-lag, flap and torsion directions respectively. The $\delta\psi$ is the virtual rotation given by

$$\delta\psi = \delta\hat{\phi} + w'\delta v' \tag{5}$$

The resultant wind velocity vector at a point $(\eta,0)$ on the blade section, located at a distance x from the hub center, is given by

$$\overline{V}\ (x,\eta) = -\overline{V}_b(x,\eta) + \overline{V}_i(x,\psi_n) + \overline{V}_G\ (x,\psi_n,\psi) - \overline{V}_h \tag{6}$$

where $\overline{V}_b$ is the blade velocity relative to the hub-fixed system, $\overline{V}_i$ is the induced flow normal to the hub plane, $\overline{V}_G$ is the gust velocity at the blade section and $\overline{V}_h$ is the hub velocity relative to the inertial frame. The $\overline{V}_h$ also includes the forward velocity vector. The detailed expressions for these velocity vectors are given in Ref. 5. Using the transformation matrices given in Appendix A the resultant wind velocity vector can be put in the form

$$\overline{V} = -\ U_R\ \overline{i}_\xi - U_T\ \overline{i}_\eta - U_p\ \overline{i}_\zeta \tag{7}$$

The velocity components, U_R, U_T, U_P are along the negative directions of the deformed coordinates (Fig. 3). Note that these velocity components are functions of the blade displacements and the azimuth position of the blade.

The airfoil characteristics are expressed as

$$\begin{aligned} C_\ell &= C_o + C_1\ \alpha \\ C_d &= d_o + d_1\,|\alpha| + d_2\ \alpha^2 \\ C_{m_{ac}} &= f_o + f_1\ \alpha \end{aligned} \tag{8}$$

Using quasisteady strip theory, and introducing correction for reversed flow, the circulatory aerodynamic forces in the deformed frame are given by

$$\begin{aligned} \overline{L}_{uc} &= -\ \frac{\rho c}{2}\,[d_o\ u_R\ |u_T| + d_1\ |u_p|\ u_R] \\ \overline{L}_{vc} &= -\ \frac{\rho c}{2}\,\text{sign}\ (u_T)\ [C_o\ u_p\ |u_T| - C_1\ u_p^2 + d_o\ (u_T^2 + u_p^2) \\ &\quad + d_1\ |u_p|\,|u_T| + d_2\ u_p^2] \end{aligned} \tag{9}$$

$$\bar{L}_{wc} = \frac{\rho c}{2} [C_o (u_T^2 + u_p^2) - C_1 u_p |u_T| - d_o u_p |u_T|$$

$$- d_1 |u_p| u_p]$$

$$M_{\phi c} = \frac{\rho c^2}{2} \text{sign } (u_T) [f_o (u_p^2 + u_T^2) - f_1 u_p |u_T|] - \bar{L}_{wc} \bar{e}_d$$

where

$$\bar{e}_d = e_d \qquad \text{(normal flow)} \tag{10}$$

$$= c + e_d - x_{ac} - (x_{ac})_{REV\ FLOW} \qquad \text{(reverse flow)}$$

Aerodynamic forces in the undeformed frame are obtained by applying the transformation

$$[L^A_{u_c} \quad L^A_{v_c} \quad L^A_{w_c}] = T_1^T [\bar{L}_{u_c} \quad \bar{L}_{v_c} \quad \bar{L}_{w_c}] \tag{11}$$

The hub-motion induced inertia force per unit volume at a point (ξ,η) in the blade section is

$$\bar{F}_h (x,\xi,\eta) = - \rho_s (x,\xi,\eta)(\ddot{x}_h \bar{i}_{\bar{x}} + \ddot{y}_h \bar{i}_{\bar{y}} + \ddot{z}_h \bar{i}_{\bar{z}}) \tag{12}$$

Integrating $\bar{F}_h$ over the blade section and using the transformation matrices T_2 and T_3, the components L^H_u, L^H_v, L^H_w, M^H_ϕ, of the hub-induced inertia at a blade section can be obtained (Ref. 5). The resultant forces along the undeformed blade coordinates are

$$\begin{aligned}
L_u(x,\psi) &= L^A_{u_c} + L^H_u \\
L_v(x,\psi) &= L^A_{v_c} + L^H_v \\
L_w(x,\psi) &= L^A_{w_c} + L^A_{wNC} + L^H_w \\
M_\phi(x,\psi) &= M^A_{\phi c} + M^A_{\phi NC} + M^H_\phi
\end{aligned} \tag{13}$$

Fuselage Equations of Motion

The equations of fuselage force equilibrium can be vectorially expressed as

$$-M(\ddot{x}_h \bar{i}_{\bar{x}} + \ddot{y}_h \bar{i}_{\bar{y}} + \ddot{z}_h \bar{i}_{\bar{z}}) + \bar{F} (\underset{\sim}{x}_h, \dot{\underset{\sim}{x}}_h, \psi) = 0 \tag{14}$$

where M is the vehicle total mass. $\bar{F}$ is the resultant of the rotor aerodynamic forces, fuselage aerodynamic forces, gravity loads, and the rotor inertia forces (excluding hub-motion induced inertia forces). The $\underset{\sim}{x}_h$ is the vector of hub dispalcements

$$\underset{\sim}{x}_h = [x_h \quad y_h \quad z_h \quad \alpha_T \quad \phi_T]^T \tag{15}$$

The vector equation governing the fuselage moment equilibrium is

$$-\frac{d}{dt}(\underset{\sim}{I}\ \overline{\omega}_h) + (-x_{cg}\ \overline{i}_{x2} + y_{cg}\ \overline{i}_{y2} - h\ \overline{i}_{z2}) \times$$

$$(\ddot{x}_h\ \overline{i}_x + \ddot{y}_h\ \overline{i}_y + \ddot{z}_h\ \overline{i}_z)\ M + \overline{Q}\ (\dot{\underset{\sim}{x}}_h,\ \underset{\sim}{x}_h,\ \psi) = 0 \tag{16}$$

where $\overline{Q}$ is the moment vector about the hub center due to the force vector $\overline{F}$. The $\underset{\sim}{I}$ is the mass-moment-of-inertia matrix about the hub center and can be written as

$$\underset{\sim}{I} = \begin{bmatrix} I_{x_1} & -I_{x_1y_1} & -I_{x_1z_1} \\ -I_{x_1y_1} & I_{y_1} & -I_{y_1z_1} \\ -I_{x_1z_1} & -I_{y_1z_1} & I_{z_1} \end{bmatrix} \tag{17}$$

The $\overline{\omega}_h$ is the hub angular velocity

$$\overline{\omega}_h = -\dot{\phi}_s\ \overline{i}_{x1} - \dot{\alpha}_s\ \overline{i}_{y1} \tag{18}$$

Induced Inflow Equations

For the steady flight state, the induced flow is assumed to be related to the rotor thrust by the relation

$$\lambda(r,\psi) = \mu \tan\alpha + \frac{C_T}{2\sqrt{\mu^2+\lambda^2}}\ (1+x\ k_x \cos\psi + x\ k_y \sin\psi)\ . \tag{19}$$

where k_x and k_y are obtained from Drees model.

For the gust-induced reponse the unsteady aerodynamic effects are introduced in an approximate manner through dynamic inflow modelling. A linear variation of the perturbed inflow is assumed

$$\delta\lambda = \delta\lambda_0 + \delta\lambda_{1c}\ x \cos\psi + \delta\lambda_{1s}\ x \sin\psi \tag{20}$$

The inflow variables are related to the unsteady aerodynamic forces and moments

$$\underset{\sim}{m}\ \delta\dot{\underset{\sim}{\lambda}} + \underset{\sim}{\ell}^{-1}\ \delta\underset{\sim}{\lambda} = [\delta C_T^A \quad -\delta C_{m_x}^A \quad \delta C_{m_y}^A]^T \tag{21}$$

where

$$\delta\underset{\sim}{\lambda} = [\delta\lambda_0 \quad \delta\lambda_{1s} \quad \delta\lambda_{1c}]^T \tag{22}$$

The coefficients of matrices $\underset{\sim}{m}$ and $\underset{\sim}{\ell}$ are adapted from Ref. 9. The elements of matrix $\underset{\sim}{\ell}$ are modified to account for the change in the air mass flow through the rotor disk caused by gust and hub motion.

Finite Element Discretization

The blade is divided into a number of beam elements. Each element consists of five nodes and fifteen nodal degrees of freedom (Fig. 4). The elemental properties are obtained by applying Hamilton's principle. The assembly of the elements, followed by imposition of the boundary conditions, yields blade equations in terms of the nodal displacements $\underset{\sim}{q}$, the inflow variables $\underset{\sim}{\lambda}$ and the hub displacements $\underset{\sim}{x}_h$:

$$[M(\underset{\sim}{q},\psi_n)] \begin{Bmatrix} \ddot{\underset{\sim}{q}} \\ \underset{\sim}{0} \\ \ddot{\underset{\sim}{x}}_h \end{Bmatrix} + [C(\underset{\sim}{q},\psi_n)] \begin{Bmatrix} \dot{\underset{\sim}{q}} \\ \underset{\sim}{0} \\ \dot{\underset{\sim}{x}}_h \end{Bmatrix} + [K(\underset{\sim}{q},\underset{\sim}{U}_G,\psi_n)] \begin{Bmatrix} \underset{\sim}{q} \\ \underset{\sim}{\lambda} \\ \underset{\sim}{x}_h \end{Bmatrix}$$

$$= \{Q_{NL}(\underset{\sim}{q},\underset{\sim}{U}_G,\psi_n\} \quad ; \quad n = 1,2,\ldots,N_b \tag{23}$$

Expressing blade forces in terms of the nodal displacements, equation (14) and (16) governing the fuselage motion can together be put in the form

$$F_H(\underset{\sim}{x}_h,\dot{\underset{\sim}{x}}_h,\ddot{\underset{\sim}{x}}_h,\underset{\sim}{\lambda},\underset{\sim}{q}^1,\underset{\sim}{q}^2,\ldots\underset{\sim}{q}^{N_b},\dot{\underset{\sim}{q}}^1,\dot{\underset{\sim}{q}}^2,\ldots,\dot{\underset{\sim}{q}}^{N_b},\psi) = 0 \tag{24}$$

where $\underset{\sim}{q}^n$ represents the nodal displacements vector for the nth blade. Similarly, the inflow equations can be expressed as

$$F_\lambda(\underset{\sim}{x}_h,\dot{\underset{\sim}{x}}_h,\dot{\underset{\sim}{\lambda}},\underset{\sim}{\lambda},\underset{\sim}{q}^1,\underset{\sim}{q}^2,\ldots,\underset{\sim}{q}^{N_b},\dot{\underset{\sim}{q}}^1,\dot{\underset{\sim}{q}}^2,\ldots,\dot{\underset{\sim}{q}}^{N_b},\underset{\sim}{U}_G,\psi) = 0 \tag{25}$$

Dynamic Stall

Dynamic stall is characterized by a delay in the flow separation due to blade motion, and by vortex shedding from the leading edge of a bade section when stall initiates. The vortex shedding induces transient loads. These features are included using a model proposed by Johnson[13]. The corrected aerodynamic coefficients are

$$C_\ell(\alpha) = \sec^2 \Lambda \, [\frac{\alpha}{\alpha_d} \{C_\ell \, (\alpha_d \cos^2 \Lambda) - C_\ell(0)\} + C_\ell(0)] + \Delta C_\ell$$

$$C_d(\alpha) = \sec \Lambda \, C_d \, (\alpha_d \cos \Lambda) + \Delta C_d \tag{26}$$

$$C_m(\alpha) = C_m \, (\alpha_d \cos^2 \Lambda) + \Delta C_m$$

where

$$\Lambda = \cos^{-1} \sqrt{\frac{U_T^2 + u_p^2}{u_T^2 + u_p^2 + U_R^2}} \tag{27}$$

The Λ is the yawed flow angle, α_d is the delayed angle of attack and ΔC_ℓ, ΔC_d, ΔC_m are the increments in the aerodynamic coefficients caused by leading-edge vortex. The angle α_d is a function of the time derivative of the angle of attack,

$$\alpha_d = \alpha - \min\left(\tau \left|\frac{\dot{\alpha} c}{u_T}\right| , \alpha_{max}\right) \operatorname{sign}(\dot{\alpha}) \tag{28}$$

where τ is the normalized time constant and its value depends on whether we are interested in C_l, C_d, or C_m. The increments ΔC_l, ΔC_d, and ΔC_m occur when the section angle of attack reaches the dynamic stall angle α_{ds} (about 3° above static stall angle) and a leading-edge vortex is shed. It is assumed that these increments build up linearily to their maxium values in an azimuth interval of 15° and then fall linearly to zero in the same azimuth interval. The peak values of ΔC_l, ΔC_d, and ΔC_m are functions of the pitch rate $\dot{\alpha}$; the expressions are given in Ref. 13. After the transient loads die out, dynamic stall does not occur unless the flow is reattached; flow reattachment occured when α falls below α_{re} (just below the static stall angle).

SOLUTION PROCEDURE

Equations (23-25), representing the rotor-fuselage dynamics, are nonlinear and involve time-dependent coefficients. There is no simple way to solve these equations directly. The problem is therefore divided into three phases: vehicle trim, steady response and gust response.

The vehicle trim solution gives the rotor control inputs and the vehicle orientation $\overset{\circ}{x}_h$ for a prescribed flight condition. The propulsive trim is obtained by solving iteratively the nonlinear equations governing the vehicle equilibrium in steady-state flight condition.

The azimuth-dependent blade equilibrium position in steady flight is calculated by first transforming the blade equations into modal space, and then solving the resulting normal-mode nonlinear equations by a procedure based on Floquet theory. Reference 14 gives details for calculating the vehicle trim and the blade equilibrium positions.

The final phase involves determining the transient response of the rotor-fuselage system due to gust loading. The response equations are linearized about the steady-state vehicle trim and the azimuth-dependent blade equilibrium position. The linearized blade and fuselage equations are described in Ref. 5. The linearized blade equations, hub equations and the dynamic inflow equations can together be put in the matrix form

$$[\overline{M}(\hat{q}^\circ,\psi)]\begin{Bmatrix}\ddot{\hat{q}}\\ \underset{\sim}{0}\\ \ddot{\underset{\sim}{x}}_h\end{Bmatrix} + [C(\hat{q}^\circ,\psi)]\begin{Bmatrix}\dot{\hat{q}}\\ \delta\dot{\underset{\sim}{\lambda}}\\ \dot{\underset{\sim}{x}}_h\end{Bmatrix} + [\overline{K}(\hat{q}^\circ,\dot{\hat{q}}^\circ,\underset{\sim}{\lambda},\underset{\sim}{U}_G,\overset{\circ}{\underset{\sim}{x}}_h,\psi)]\begin{Bmatrix}\hat{q}\\ \delta\underset{\sim}{\lambda}\\ \underset{\sim}{x}_h\end{Bmatrix}$$

$$= \{\overline{Q}(\hat{q}^\circ,\underset{\sim}{x}_h^\circ,\underset{\sim}{U}_G,\psi)\} \tag{29}$$

where

$$\{\hat{q}\} = [\underset{\sim}{q}^1\ \underset{\sim}{q}^2\ \dots\ \underset{\sim}{q}^{N_b}]^T \tag{30}$$

Note that the stiffness matrix $\overline{K}$ is a function of $\underset{\sim}{\lambda}$ and $\underset{\sim}{U}_G$. This implies that the gust field $\underset{\sim}{U}_G$ can alter the stability of the basic system.

Equations (29) are transformed to the modal space using the first few (M) natural modes for the blade. The coupled normal mode response equations can be written as

$$[M^*]\{\ddot{p}\} + [C^*]\{\dot{p}\} + [K^*(\underset{\sim}{\lambda},\underset{\sim}{U}_G)]\{p\} = \{Q^*(\underset{\sim}{U}_G)\} \tag{31}$$

The size of the vector $\{p\}$ is MN_b+8; this includes three variables for dynamic inflow and five for the hub motion. Equation (31) is solved numerically using a time integration technique for a specified gust field.

Blade bending moments

From the solution vector $\{p\}$, we can obtain the blade displacements, u,v,w,ϕ, the dynamic inflow variables λ, and the hub displacements x_h. Using this information, we calculate the blade section force components L_u, L_v, L_w and M_ϕ for each blade. Note that each of these components consists of three parts: the aerodynamic forces, the hub-motion induced inertia forces and the blade-motion induced inertia forces Equations (7-13) are used to calculate the aerodynamic and hub-motion induced forces. The procedure for finding the blade-motion induced inertia forces is given in Ref. 15.

Force summation method is employed to calculate the root moment vector

$$\overline{M}_{ROOT} = \int_0^R [\overline{i}_x(-L_v\, w + L_w\, v) + \overline{i}_y\,(L_u\, w - L_w\,(r+u))$$

$$+ \overline{i}_z\,(-L_u\, v + L_v\,(r+u)) + M_\phi\, \overline{i}_\xi]dr \qquad (32)$$

Hub forces and moments

$$F_{x_H} = \sum_{n=1}^{N_b} \int_0^R (L_u^n \cos\psi_n - L_v^n \sin\psi_n - L_w^n \cos\psi_n\, \beta_p)\, dr$$

$$F_{y_H} = \sum_{n=1}^{N_b} \int_0^R (L_u^n \sin\psi_n + L_v^n \cos\psi_n - L_w^n \cos\psi_n\, \beta_p)\, dr \qquad (33)$$

$$F_{z_H} = \sum_{n=1}^{N_b} \int_0^R (L_u^n\, \beta_p + L_w^n)\, dr$$

$$M_{x_H} = \sum_{n=1}^{N_b} [M_x \cos\psi_n - M_y \sin\psi_n - M_z \cos\psi_n\, \beta_p + \int_0^R M_\phi$$

$$\cdot \{(1 - \frac{v'^2+w'^2}{2}) \cos\psi_n - v'\sin\psi_n - w'\cos\psi_n\, \beta_p\}dr]^{(n)}$$

$$M_{y_H} = \sum_{n=1}^{N_b} [M_x \sin\psi_n - M_y \cos\psi_n - M_z \cos\psi_n\, \beta_p + \int_0^1 M_\phi$$

$$\cdot \{(1 - \frac{v'^2+w'^2}{2}) \sin\psi_n + v'\cos\psi_n + w'\sin\psi_n\, \beta_p\}dr]^{(n)}$$

$$M_{z_H} = \sum_{n=1}^{N_b} [M_x \ \beta_p + M_z + \int_0^R M\phi \ \{1 - \frac{v'^2+w'^2}{2}) \ \beta_p + w'\}dr]^{(n)}$$

where

$$M_x = \int_0^R (-L_v \ w + L_w \ v)dr$$

$$M_y = \int_0^R (-L_u \ w - L_w \ (r+u))dr \qquad (34)$$

$$M_z = \int_0^R (-L_u \ v + L_v \ (r+u))dr$$

RESULTS AND DISCUSSION

The gust-induced response is examined for a four-bladed hingeless rotor with Lock number $\gamma = 5$, thrust level $C_T/\sigma = 0.1$, solidity ratio $\sigma = .05$ and zero precone. The blade airfoil static characteristics are taken as

$$C_\ell = 6.28 \ \alpha \ , \quad \alpha \leq 12°$$

$$= 1.315 \ , \quad \alpha > 12°$$

$$C_d = .0095$$

$$C_m = 0$$

These characteristics get modified somewhat by dynamic stall effects. The delayed lift, drag and moment coefficients are calculated using time lag factors τ_L of 4.8, τ_D of 2.7 and τ_M of 2.7. The dynamic stall angle is assumed to be 15° (3° above the static stall angle). The peak values of the vortex-induced increments in lift, drag and moment coefficients are: $\Delta C_\ell = 2.0$, $\Delta C_d = 0$ and $\Delta C_m = -.65$. The flow reattachment is assumed to take place at the static stall angle.

The fuselage c.g. lies on the shaft axis and is located at a distance 0.2R below the hub center. The fuselage drag coefficient in terms of flat plate area $(f/\pi R^2)$ is taken as 0.1. The inertia properties of the fuselage are given in Table 1. The blade properties are assumed uniform an these are also given in Table 1. The stiffness values EI_y, EI_z and GJ and the inertia parameters, k_{m1} k_{m2} and K_A are chosen so as to yield the desired blade frequencies. The fundamental flap and torsion frequencies are 1.15/rev and 5.0/rev respectively. Two values of the lag bending frequency are used: 0.7/rev for the soft-inplane rotor and 1.5/rev for the stiff-inplane rotor.

Response in hover

To examine the sensitivity of the gust response to various parameters, a simple gust model is first used. The gust is uniform, vertical and its magnitude in terms of the blade tip speed $(W_G/\Omega R)$ is 7%. (For example, for a tip speed of 700 fps, the gust velocity would be about 50 fps.) It hits the rotor suddenly at $\psi = 0$; ψ represents the nondimensionalized time in terms of rotor cycles. The effects of dynamic infow, dynamic stall and reverse flow are included in all the results unless otherwise mentioned.

Figure 5 shows flap, lag and torsion bending deflections at the blade tip for the soft-inplane rotor. The flap response builds up to its peak value ($\approx$ 5.4% R) in 0.4 cycle and the oscillations in the subsequent response die out quickly. The lag response is quite comparable with the flap response and decays out rather slowly. The torsion response is much smaller and appears weakly coupled with the lag response. Figure 6 presents the variations of the thrust ratio and the load factor for the same soft-inplane rotor. The thrust ratio is the ratio of the instantaneous rotor aerodynamic thrust to the steady-state thrust. The rotor thrust jumps to about 1.85 times the steady-state value when the gust first hits the rotor. The thrust then falls rapidly due to the relieving effect of the flap motion. The subsequent thrust variation is due to the combined effect of the aerodynamic foce, dynamic inflow and the blade motion. The second thrust peak is higher than the first one. If the effect of dynamic stall is neglected (Ref. 5), the first peak becomes larger than the second. The load factor is the ratio of the vertical force experienced by the fuselage to the gross weight of the vehicle. The load factor attains its minimum value at ψ = 0, and this value is slightly less than unity implying that the fuselage experiences a mild download. Initially the load factor variation is out of phase with the thrust variation, but later becomes in phase with it. The maximum load factor exceeds the peak thrust value implying the importance of the blade inertia forces. Figures 7(a) and 7(b) respectively present the flap bending moment (M_η) and the lag bending moment (M_ζ) induced at the blade root. The dotted line shows the steady-state moment and the full line presents the total moment consisting of the steady and the gust-induced components. These moments have been nondimensionalized with respect to $m_o\Omega^2R^3$. The peak amplitude of the total flap bending moment is about 1.8 times the steady-state value. On the other hand, the peak amplitude of the total lag bending moment is about four times the steady-state value and acts in a direction opposite to that of the steady lag moment. The variations of the flap and lag bending moments appear to be in phase with the flap and lag deflections respectively.

Figures 8(a) - 8(e) show the effect of dynamic stall on the peak gust-induced response values for different thrust levels. For $C_T/\sigma >$ .1, the gust velocity induces dynamic stall condition on the blades. As the thrust level increases, the stall region becomes larger causing a reduction in both the aerodynamic thrust and the blade bending moments. As a result of these reductions, the peak flap deflection and the peak load factor values are also reduced at higher thrust levels.

Figures 9, 10(a) and 10(b) present results for the stiff-inplane rotor. Figure 9 shows the time variation of the gust-induced blade tip deflections. Comparing results with the soft-inplane case, the flap oscillations appear to be somewhat less damped. The lag response, however, decays more quickly. The coupling between the lag and pitch motions appears to be stronger than that observed for the soft-inplane rotor. The flap bending moment variation, shown in Fig. 10(a), is quite similar to that for the soft-inplane rotor. However, the lag bending moment variation, plotted in Fig. 10(b), is quite different from that for the soft-inplane rotor. Both the steady-state lag moment and peak value of the total lag moment are about three times their respective values for the soft-inplane rotor.

Figures 11(a) and 11(b) show the root bending moment variations for the soft-inplane rotor which is suddently submerged in a lateral gust at time ψ = 0. The lateral gust velocity is 7% of the rotor speed. Results are presented for blade 1 which is located at the rearward position when the gust first hits the rotor (time ψ = 0). The flap bending moment, plotted in Fig. 11(a), builds up to about 1.4 times the steady-state value in three cycles, and then decays out slowly. The lag bending moment variation, shown in Fig. 11(b), has a very small magnitude, but the oscillations persist for a long time. Note that the frequency of flap and lag moment variations tends to 1/rev as time progresses.

Gust reponse in forward flight

The propulsive trim state of the vehicle in steady forward flight is first calculated by solving the vehicle equilibrium equations. Then, the blade azimuth-dependent steady deflection is obtained using the Floquet theory. Finally, the rotor-fuselage gust response is calculated for a given gust input. Results are presented for vertical and lateral gusts, and the same vehicle characteristics as used in hover are retained.

Figures 12-24 show forward flight results for a uniform vertical gust having a velocity of 7% of the rotor tip speed. Figures 12-16 present results for a soft-inplane rotor moving at an advance ratio of 0.2. The gust hits the rotor at time ψ = 0. In forward flight, the rotor inflow pattern is not axisymmetric and therefore the response of each blade is different. However, the overall response trends for different blades are quite similar. Figure 12 shows the flap, lag and torsion deflections at the tip of blade 1. Comparing results with those obtained in hover (Fig. 5) the initial flap response for about one cycle appears quite similar, but the subsequent transient response is of much larger amplitude and dies out at a much slower rate. The lag response is about twice that observed in hover. The pitch response is also somewhat higher in forward flight. It was noticed that if the dynamic stall effects were not included, negative values of the perturbation flap response were not observed. Figure 13 shows that thrust ratio and load factor variations at the same advance ratio of 0.2. Comparing with the results obtained in hover (Fig. 6) we note that the initial peak thrust value is the same for both the cases and that the second peak value is smaller in forward flight. The subsequent thrust level however remains higher and oscillations persist for a longer period in forward flight. Simlar remarks apply to the load factor variation. Figs. 14(a) and (14(b) respectively present the variations in the flap bending moment and the lag bending moment. The mean value of the steady-state flap response is almost the same as observed in hover (Fig. 7a), whereas the gust-induced flap response is quite different from that observed in hover. Also, the gust-induced flap moment and the flap deflections appear to be in phase. We further notice that the total fap moment variation tends to become in phase with the steady-state variation as time progresses. Figure 14(b) shows the lag bending moment response. The mean value of the steady-state response is almost zero whereas its peak-to-peak amplitude is about twice that of the steady-state flap moment. The total lag moment amplitude is however about one-half the total lag moment amplitude. Like the flap response, the lag response also tends to get in phase with the steady-state response as time passes. Figure 15 shows the hub moment variations with time. The pitching moment is positive nose-up and the rolling moment is positive advancing-side-up. The hub moments have been nondimensionalized with respect to $m_o \Omega^2 R^3$. Both the pitching and the rolling moments for the 4-bladed rotor show 4/rev fluctuations in their time histories. Figure 16 shows the gust-induced wobbling of the rotor tip path plane. The horizontal axis represents the longitudinal tilt (equivalent to β_{1c}) and a negative value means a rearward tilt of the disk. The vertical axis represents the lateral tilt (equivalent to β_{1s}) and a positive value means advancing-side-up. The time history of the tilt shows that the rotor disk wobbles in a progressive mode for about two cycles and the tilt attains the maximum value. Thereafter, the disk slowly returns to its steady-state position in a regressive mode. The maximum gust-induced tilts are 2° rearward and 1.4° advancing-side-down.

Figure 17 shows tip deflections for blade 1 at an advance ratio of 0.4. Comparing results with those obtained for the advance ratio of 0.2 (Fig. 12) the flap response amplitude appears larger and it decays at a much slower rate. The lag response amplitude builds up during the first five cycles (figure shows only three cycles) and thereafter decays slowly. The pitch response amplitude increases appreciably and is weakly coupled with the lag response. Figures 18(a) and 18(b) show the bending moment variations at the root of blade 1 at the advance ratio of 0.4. The mean values of steady-state moments are only slightly effected but the vibratory components are increased substantially at higher forward speeds. Comments simlar to those for the lower forward speed apply to the total flap and lag moment variations. However, the lag moment increases more rapidly than the flap moment as the forward speed increases. In fact, at the advance ratio of 0.4 the maximum lag moment (5th peak, not shown) exceeds the peak flap moment.

Figures 19-21 show results for the stif-inplane rotor at an advance ratio of 0.2. Tip deflections of blade 1 are plotted in Fig. 19. Comparing with the results for the soft-inplane rotor (Fig. 12), the flap response appears slightly reduced and the lag response appears reduced to one-third the previous value. The pitch response is somewhat increased owing to a strong coupling between the lag and pitch motions. As time passes the 5/rev fluctuations in the pitch response die out and only the lag-coupled response persists. Figure 20(a) shows the root flap moment variation for blade 1 and is quite similar to that for the soft-inplane rotor (Fig. 14a). Lag bending moment response is plotted in Fig. 20(b) and comparison with the soft-inplane results (Fig. 14b) shows that the steady-state as well as the total moment values have predominant 2/rev components. Figure 21 presents variations of the hub pitching and rolling moments. The pitching moment always remains positive and achieves its maximum value in 1.7 cycle. The rolling moment attains its maximum value in 1.5 cycle and is one-half of that observed for the pitching moment. Contrary to what is observed for the soft-inplane rotor (Fig. 15) the pitch and roll moments start dropping rapidly after achieving their maximum values. The 1/rev component of the roll moment however persists for quite some time.

Figures 22 and 23 present results for the stiff-inplane rotor at a high forward speed (μ = .4). Figure 22 shows variations of the blade tip deflections and these are quite different from those observed for the soft-inplane rotor at the same forward speed (Fig. 17). Fluctuations in the response values are rather erratic. Figure 23(a) shows the flap bending moment response. The steady-state moment has a 2/rev component of appreciable magnitude and the total moment variation is somewhat similar to that observed for the soft-inplane rotor (Fig. 18a). On the other hand, the lag moment response, shown in Fig. 23b, is very different from that for the soft-inplane rotor. Both the steady-state and the total response values primarily consist of 2/rev components. At high forward speeds, the gust can induce large flatwise stresses. For this case, the lag moment far exceeds the flap moment (2.5 times).

Figures 24(a) and 24(b) show the variation of the bending moments induced by different types of gusts for an advance ratio of 0.2. The first type represents a sudden penetration into a uniform gust field (discussed earlier), the second type represents a gradual penetration into a step gust field, and the third type represents a gradual penetration into a sine-squared gust of finite length (2R). All the gust fields have a maximum amplitude of 7% of the blade tip speed. As expected with the gradual penetration into gust field the first peak occurence is delayed. Also, gradual penetration into the sine-squared gust field results in the lowest bending moment levels. For this case, the amplitude of the flap moment gradually increases as the rotor disk enters the gust field, reaches its highest value when the disk is fully engulfed in the gust, and then starts dropping as the disk moves out of the gust region. The oscillating lag moment however persists for a long time for this case.

Figure 25 presents variation of root moments for a step lateral gust with a magnitude of 7% of rotor tip speed. The vehicle is moving at an advance ratio of 0.2 and the lateral inplane gust penetrates the disk plane gradually from the left side (retreating side). The bending response appears to contain 1/rev, 2/rev and 3/rev components. The response amplitude increases for about 4.5 cycles, which is the time taken by the gust to fully engulf the rotor, and then it decreases slowly. The results however are presented for three cycles only. Comparing with the vertical gust results (Figs. 24), the effect of lateral gust on dynamic stresses is much smaller. Figure 26 presents variation of bending moments at the higher advance ratio of 0.4. As expected, the gust-induced stresses become larger with higher forward speed.

CONCLUSIONS

The gust-induced transient response of the rotor-fuselage system is calculated both in hover and forward flight using finite element formulation. Response is calculated in terms of blade deflections, blade moments, rotor thrust, fuselage load factor, hub moments and disk tilt. The primary emphasis is however on the determination of blade bending moments. Based on this study, the following conclusions are drawn.

1. Soon after the vehicle encounters a vertical gust the blades respond immediately absorbing the initial impact of the gust, and the load transmitted to the fuselage is small. In fact, at the instant the gust hits the helicopter, the fuselage experiences a mild download whereas the rotor thrust is almost twice the steady-state value. The peak load transmitted to the fuselage may exceed the peak thrust value.

2. The second thrust peak can be larger than the first one.

3. Dynamic stall effects are important for accurate determination of gust response, particularly for higher thrust levels.

4. At low speeds, the gust-induced flap moments are dominated by low-frequency components. At higher speeds, the high-frequency components become important, more so for the stiff-inplane rotors. Also the moment levels increase with forward speed.

5. Like flap moments, gust-induced lag moments are also dominated by low-frequency components at low forward speeds. Again, at high forward speeds, and particularly for stiff-inplane rotors, the high-frequency components become important. For low forward speeds, the lag moments are smaller but comparable with the flap moments. For high speeds, the lag moments become much larger than the flap moments, especially so for stiff inplane rotors. Further, the 2/rev and 3/rev components are more prominent in the lag moment variation than in the flap moment variation.

6. Gust penetration rate and gust profile can substantially influence the response behavior of the system. Higher penetration rates and sharp-edged gust profiles cause the peak response values to occur earlier.

7. A rotor suddenly engulfed by an inplane gust experiences appreciable flap bending moment, comparable to that experienced with the vertical gust. Also, the oscillatory flap moment persists for a long time. The lag moment is much smaller for this case. If the inplane gust gradually advances over the disk, the flap and lag moment levels are much smaller compared to those caused by an upgust. The 2/rev and 3/rev components in the moment variations become quite noticeable for this case.

ACKNOWLEDGEMENT

This research work is supported by NASA Langley Research Center under NASA Grant NAG-1-375. The authors acknowledge helpful discussions with Wayne Mantay who is also Technical monitor of this grant.

REFERENCES

1. Arcidiacono, P. J., Bergquist, R. R. and Alexander, W. T., Jr., "Helicopter Gust Response Characteristics Including Unsteady Aerodynamic Stall Effects," Journal of AHS, 34, Oct. 1974.

2. Azuma, A. and Saito, S., "Study of Rotor Gust Reponse by Means of the Local Momentum Theory," Journal of AHS, Jan. 1982, pp. 58-72.

3. Yasue, M., Vehlow, C. A., and Ham, N. D., "Gust Response and Its Alleviation for a Hingeless Helicopter Rotor in Cruising Flight," Fourth European Rotorcraft and Powered Lift Aircraft Forum, Stressa, Italy, Sept. 13-15, 1978.

4. Johnson, W., "Dynamics of Tilting Proprotor Aircraft in Cruise Flight," NASA TN D-7677, May 1974.

5. Bir, G. S. and Chopra, I., "Gust Response of Hingeless Rotors," paper presented at the 41st Annual National Forum of the American Helicopter Society, Fort Worth, Texas, May 15-17, 1985.

6. Judd, M. and Newman, S J., "An Analysis of Helicopter Rotor Response Due to Gusts and Turbulence," Vertica, Vol. 1, 1977, pp. 179-188.

7. Gaonker, G. H. and Hohenemser, K. H., "Flapping Respone of Lifting Rotor Blades to Atmospheric Turbulence," J. of Aircraft, Vol. 6, No. 6, Nov.-Dec. 1969, pp. 496-503.

8. Drees, J. M. and Harvey, K. W., "Helicopter Gust Response at High Forward Speed," J. of Aircrat, Vol. 7, No. 3, May-June 1970, pp. 225-230.

9. Pitt, D. M. and Peters, D. A., "Theoretical Prediction of Dynamic Inflow Derivatives," Vertica, Vol. 5, No. 1, 1981.

10. Sivaneri, N. T. and Chopra, I., "Dynamic Stability of a Rotor Blade Using Finite Element Analysis," AIAA Journal, Vol. 20, No. 5, May 1982, pp. 716-723.

11. Sivaneri, N. T. and Chopra, I., "Finite Element Analysis for Bearingless Rotor Blade Aeroelasticity," Journal of AHS, Vol. 29, No. 2, April 1984, pp. 42-51.

12. Hong, C. and Chopra, I., "Aeroelastic Stability of a Composite Blade," Journal of the American Helicopter Society," Vol. 30, No. 2, April 1985.

13. Johnson, W., "A Comprehensive Analytical Model of Rotorcraft Aerodynamics and Dynamics: Part I," NASA TM-81182, USAAVRADCOM TR 80-A-5, June 1980.

14. Panda, B. and Chopra, I., "Dynamic Stability of Hingeless and Bearingless Rotors in Forward Flight," presented at the International Conference on Rotorcrat Basic Research, Research Triangle Park, North Carolina, Feb. 19-21, 1985.

15. Bir, G. S., "Gust Response of Hingeless and Articulated Rotors in Hover and Forward Flight," Ph.D. Dissertation, Dept. of Aerospace Engineering, University of Maryland, Sept. 1985.

APPENDIX A

The transformation between the various coordinate systems (Figs. 1 and 2) is governed by the following relations

$$\begin{Bmatrix} \bar{i}_\xi \\ \bar{i}_\eta \\ \bar{i}_\zeta \end{Bmatrix} = T_1 \begin{Bmatrix} \bar{i}_x \\ \bar{i}_y \\ \bar{i}_z \end{Bmatrix}, \quad \begin{Bmatrix} \bar{i}_{xH} \\ \bar{i}_{yH} \\ \bar{i}_{zH} \end{Bmatrix} = T_2 \begin{Bmatrix} \bar{i}_x \\ \bar{i}_y \\ \bar{i}_z \end{Bmatrix}, \quad \begin{Bmatrix} \bar{i}_{\bar{x}} \\ \bar{i}_{\bar{y}} \\ \bar{i}_{\bar{z}} \end{Bmatrix} = T_3 \begin{Bmatrix} \bar{i}_{xH} \\ \bar{i}_{yH} \\ \bar{i}_{zH} \end{Bmatrix}$$

where

$$T_1 = \left[\begin{array}{c|c|c} 1 - \frac{v'^2}{2} - \frac{w'^2}{2} & v' & w' \\ -(v'\cos\theta_1 + w'\sin\theta_1) & (1 - \frac{v'^2}{2})\cos\theta_1 - v'w'\sin\theta_1 & (1 - \frac{w'^2}{2})\sin\theta_1 \\ v'\sin\theta_1 - w'\cos\theta_1 & -1(1 - \frac{v'^2}{2})\sin\theta_1 - v'w'\cos\theta_1 & (1 - \frac{w'^2}{2})\cos\theta_1 \end{array}\right]$$

$$T_2 = \begin{bmatrix} \cos\psi_n \cos\beta_p & -\sin\psi_n & -\cos\psi_n \sin\beta_p \\ \sin\psi_n \cos\beta_p & \cos\psi_n & -\sin\psi_n \sin\beta_p \\ \sin\beta_p & 0 & \cos\beta_p \end{bmatrix}, \quad T_3 = \begin{bmatrix} 1 & 0 & -\alpha_T \\ 0 & 1 & \phi_T \\ \alpha_T & -\phi_T & 1 \end{bmatrix}$$

TABLE 1

Hingeless Blade and Fuselage Structural Properties

$EI_y/m_o\Omega^2R^4$	$= 0.014486$
$EIz/mo\Omega^2R^4$	$= 0.026655$
$GJ/m_o\Omega^2R^4$	$= 0.005661$
k_{m1}/R	$= 0$
k_{m2}/R	$= 0.025$
k_A/R	$= 0.025$
e_g/C	$= 0$
e_A/C	$= 0$
e_d/C	$= 0$
m/m_o	$= 1.0$
I_{xH}/MR^2	$= 0.09$
I_{yH}/MR^2	$= 0.12$

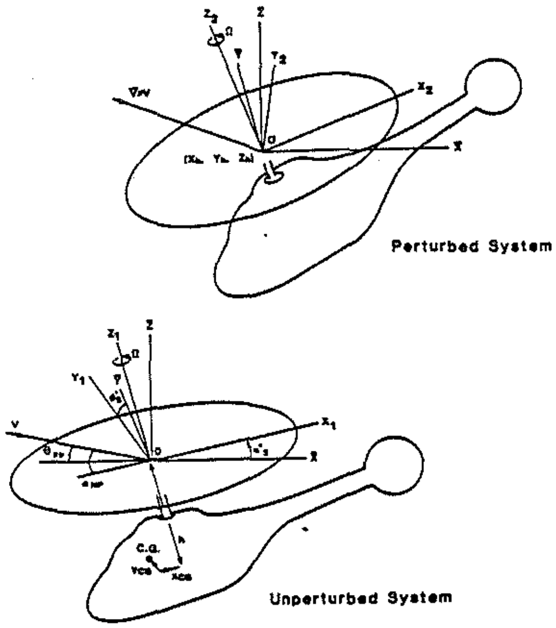

Fig. 1 Coordinate systems

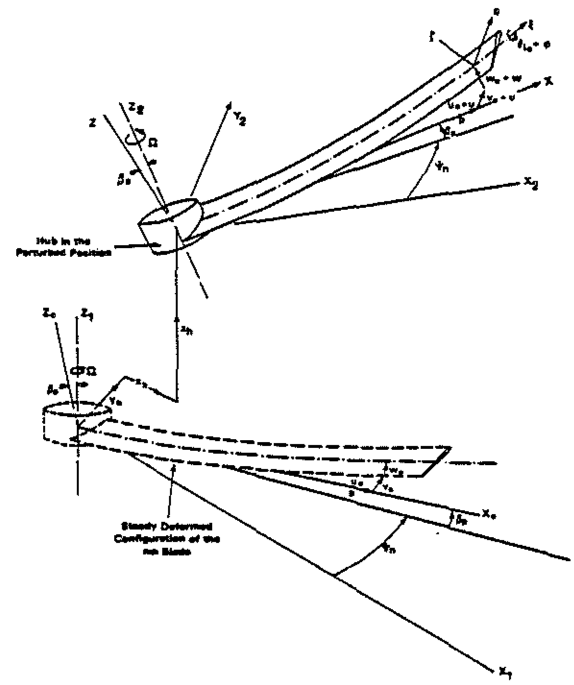

Fig. 2 Blade deflected positions

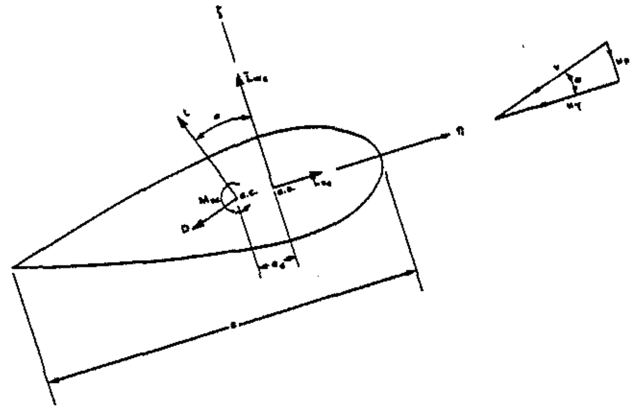

Fig. 3 Blade section aerodynamic environment

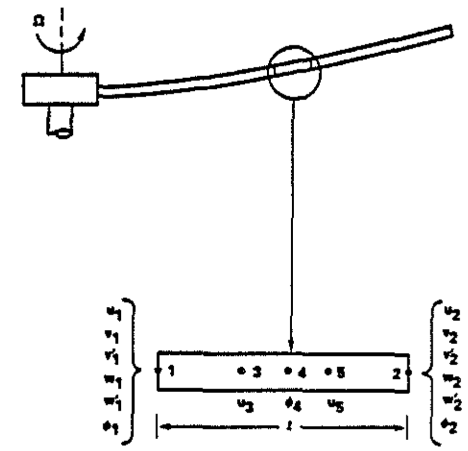

Fig. 4 Finite element model showing nodal degrees of freedom

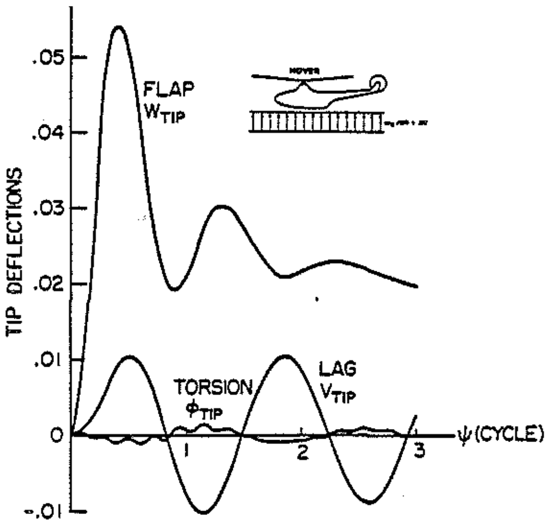

Fig. 5: Flap, lag and torsion deflections at the blade tip (nondimensionalized wrt radius) for soft-inplane rotor (ν_v = 0.7, ν_w = 1.15, ν_ϕ = 5.0).

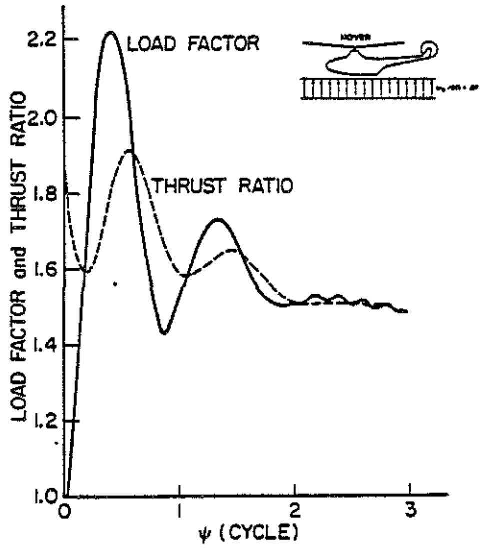

Fig. 6: Dynamic response of soft-inplane rotor in hover.

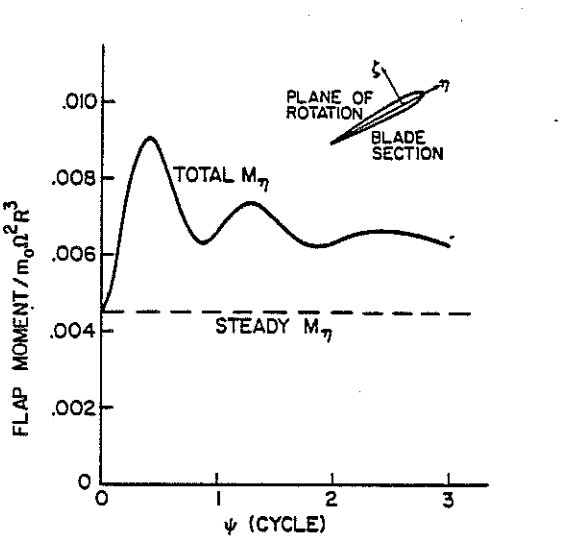

Fig. 7a: Flap moment at the blade root for soft-inplane rotor (hover).

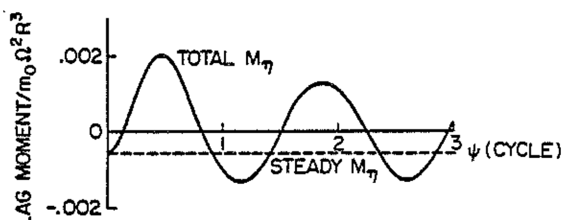

Fig. 7b Lag moment

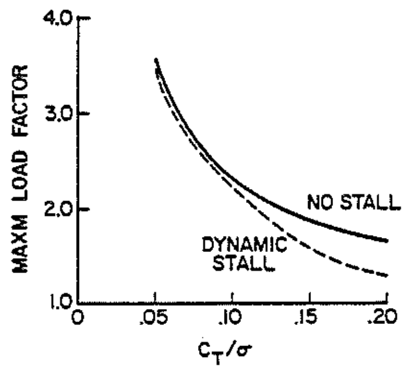

Fig. 8b: Effect of thrust loading on the peak load factor

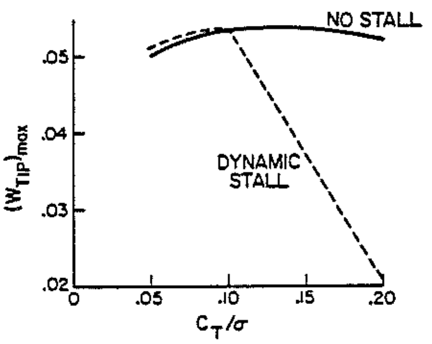

Fig. 8a: Effect of thrust loading on the peak flap deflection (soft-inplane rotor in hover)

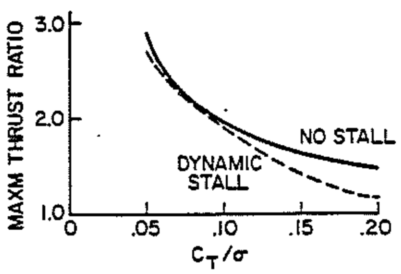

Fig. 8c: Effect of thrust loading on the maximum rotor thrust

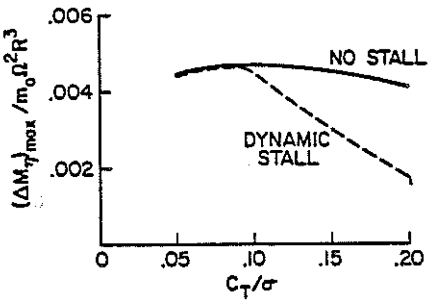

Fig. 8d: Effect of thrust loading on the maximum gust-induced flap moment

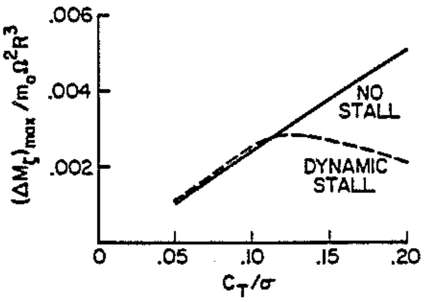

Fig. 8e: Effect of thrust loading on the maximum gust-induced lag moment

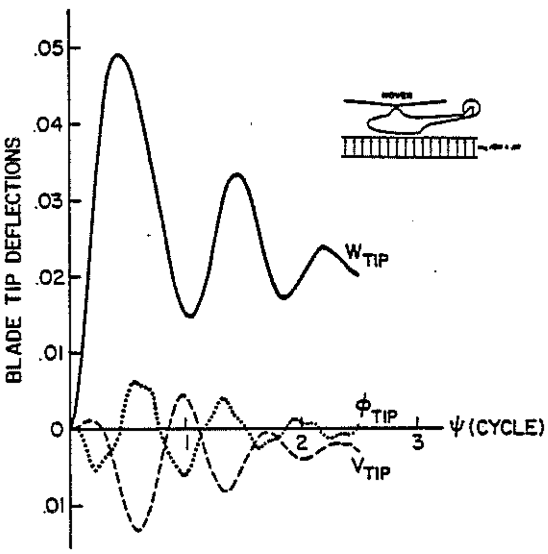

Fig. 9: Flap, lag and torsion bending deflections at the blade tip for stiff-inplane rotor (ν_v = 1.5, ν_w = 1.15, ν_ϕ = 5.0).

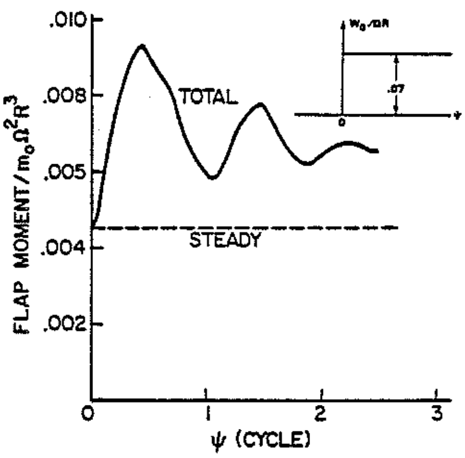

Fig. 10a: Flap moment at the blade root for stiff-inplane rotor (hover).

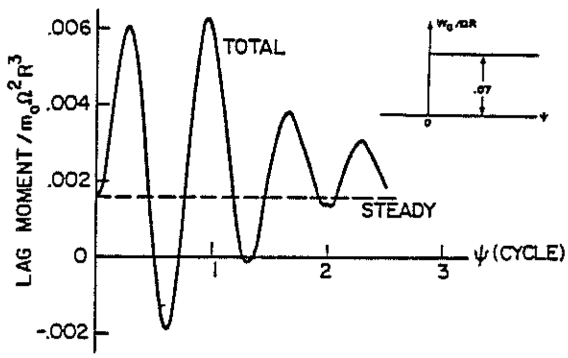

Fig. 10b: Lag moment at the blade root for stiff-inplane rotor (hover).

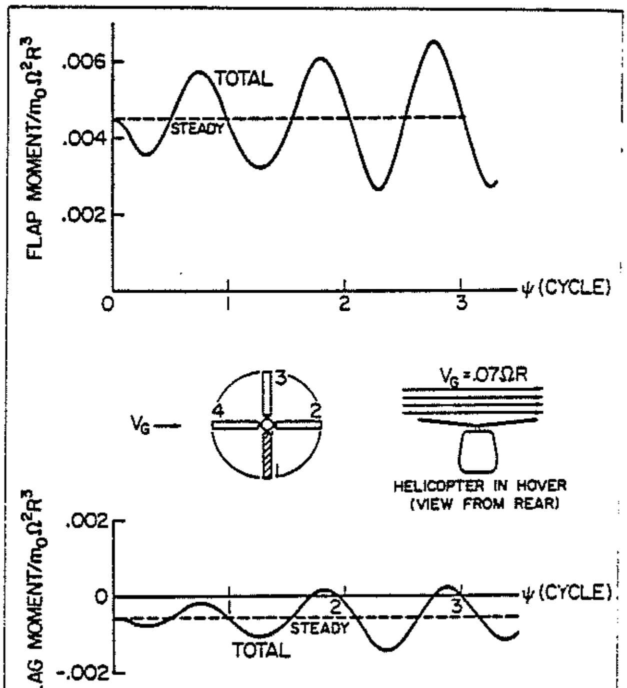

Fig. 11: Flap and lag moments at the root of blade 1 (lateral inplane gust suddenly hitting the soft-inplane rotor in hover).

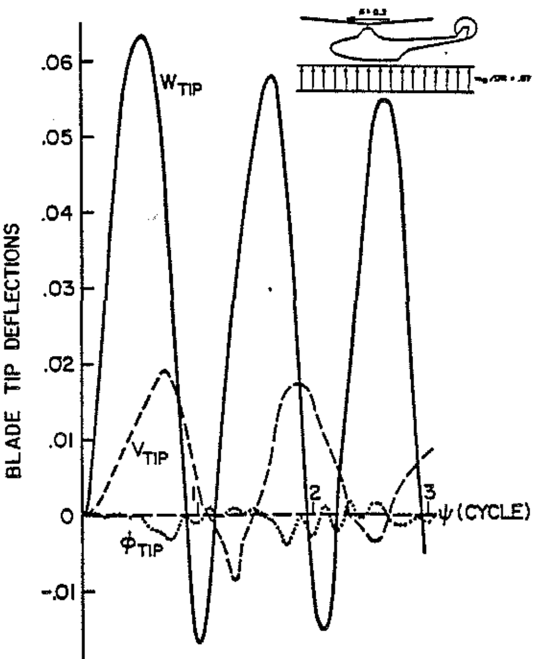

Fig. 12: Flap , lag and torsion deflections at the tip of blade 1 for soft-inplane rotor (μ = .2).

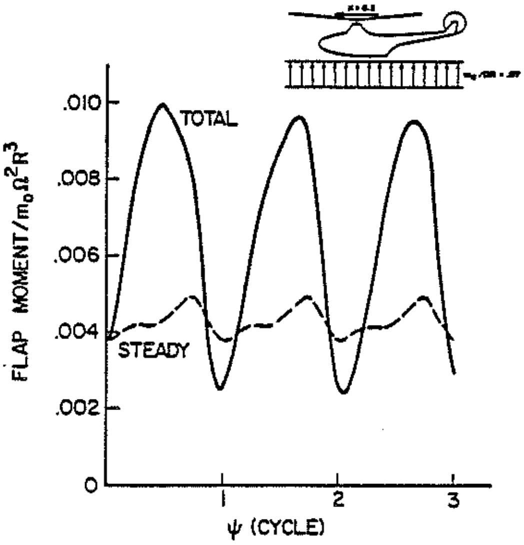

Fig.14a: Flap moment at the root of blade 1 for soft-inplane rotor (μ = .2).

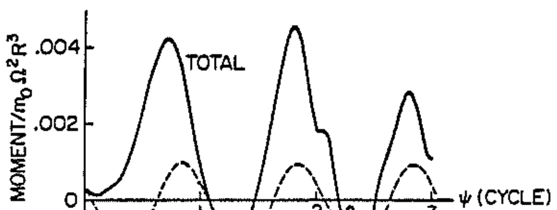

Fig. 14b: Lag moment at the root of blade 1

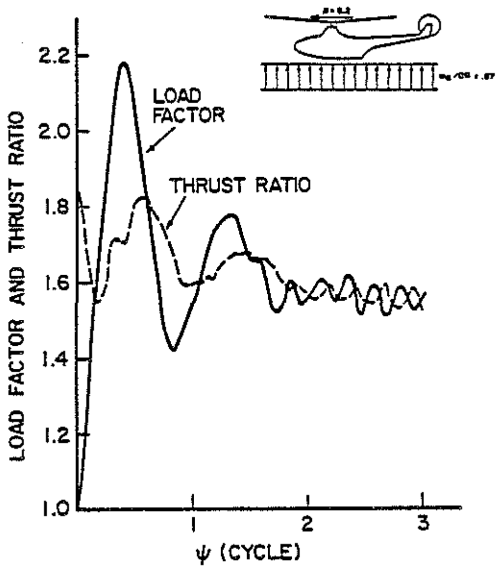

Fig. 13: Dynamic response of soft-inplane rotor.

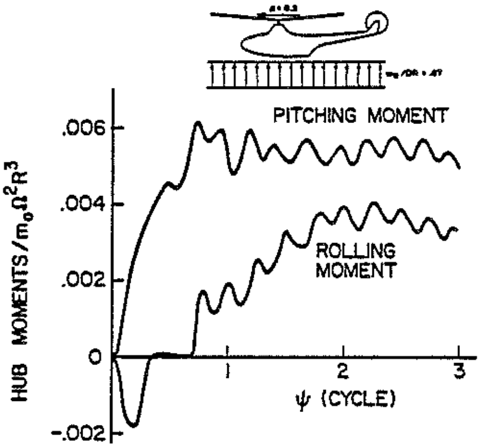

Fig. 15: Time variation of hub pitching and rolling moments for soft-inplane rotor (μ = 0.2).

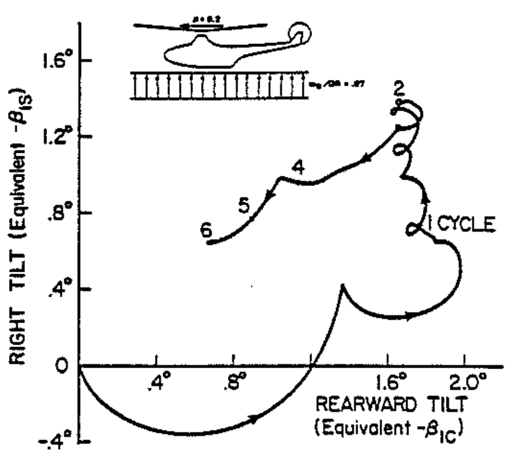

Fig. 16: Time variation of disk tilt for soft-inplane rotor (μ = 0.2).

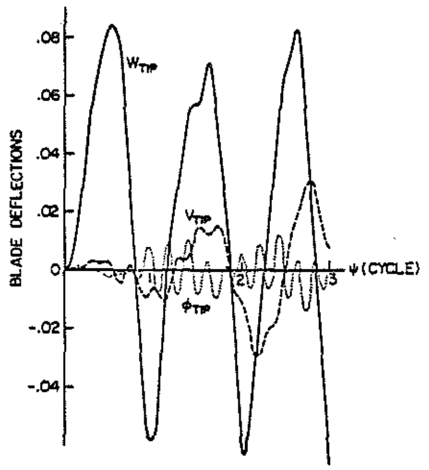

Fig. 17: Flap, lag and torsion deflections at tip of blade 1 for soft-inplane rotor (μ = 0.4).

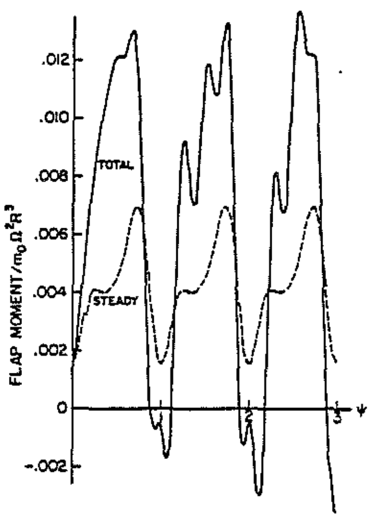

Fig. 18a: Flap moment at the root of blade 1 for soft-inplane rotor (μ = 0.4).

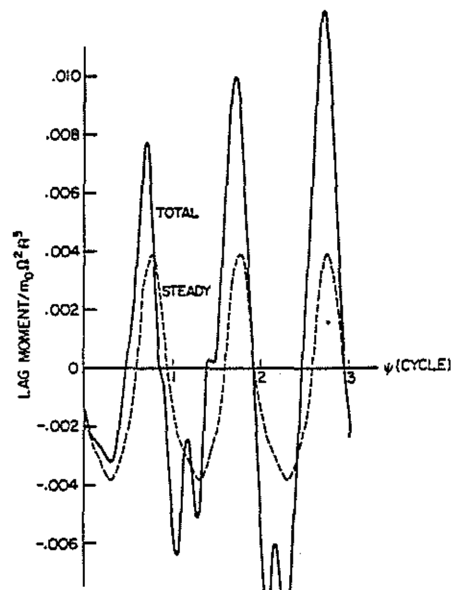

Fig. 18b: Lag moment at the root of blade 1 for soft-inplane rotor (μ = 0.4).

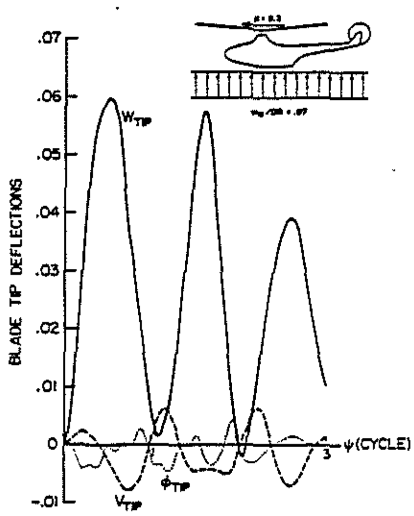

Fig. 19: Flap, lag and torsion deflections at the tip of blade 1 for stiff-inplane rotor (μ = 0.2).

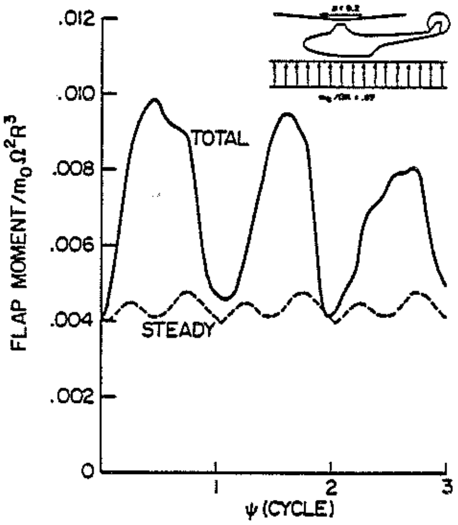

Fig. 20a: Flap moment at the root of blade 1 for stiff-inplane rotor (μ = 0.2).

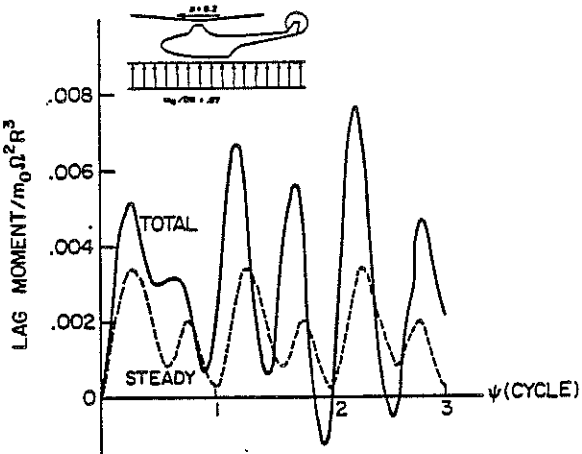

Fig. 20b: Lag moment at the root of blade 1 for stiff-inplane rotor (μ = 0.2).

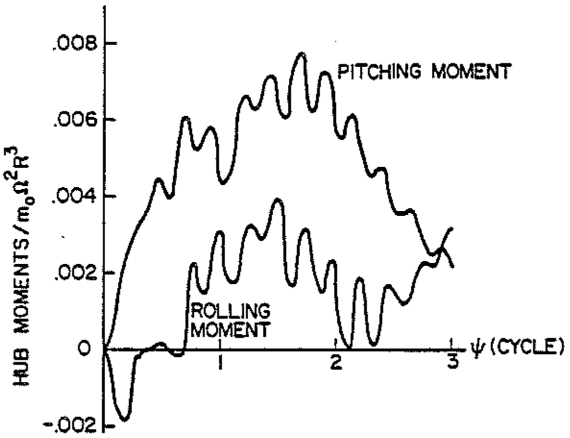

Fig. 21: Hub pitching and rolling moments for stiff-inplane rotor (μ = 0.2).

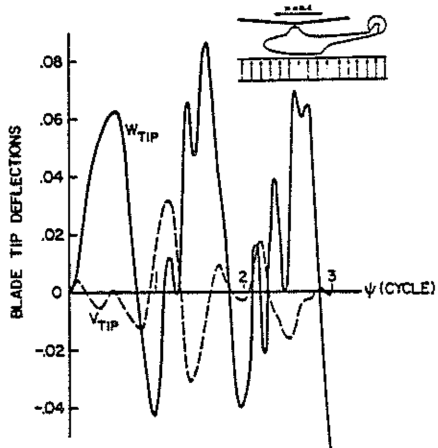

Fig. 22: Flap, lag and torsion deflections at the tip of blade 1 for stiff-inplane rotor (μ = 0.4).

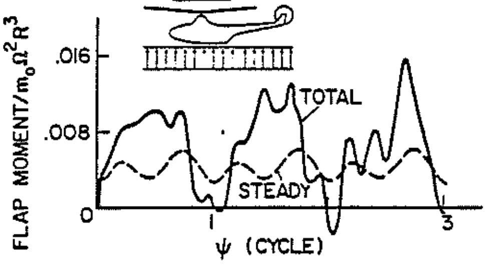

Fig. 23a: Flap moment at the root of blade 1 for stiff-inplane rotor (μ = 0.4).

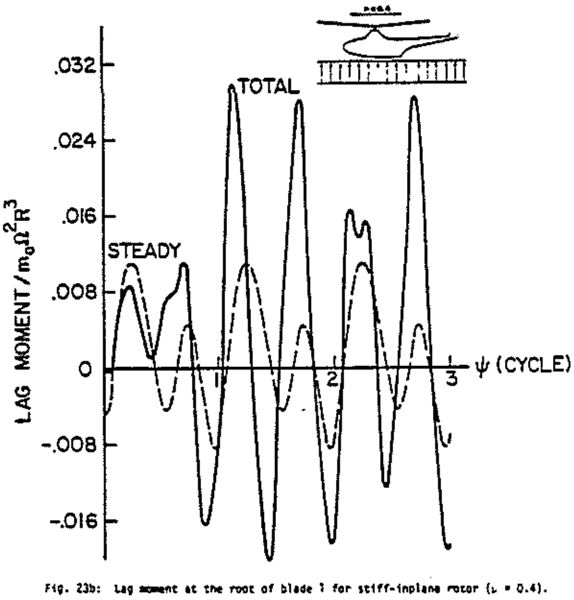

Fig. 23b: Lag moment at the root of blade 1 for stiff-inplane rotor (μ = 0.4).

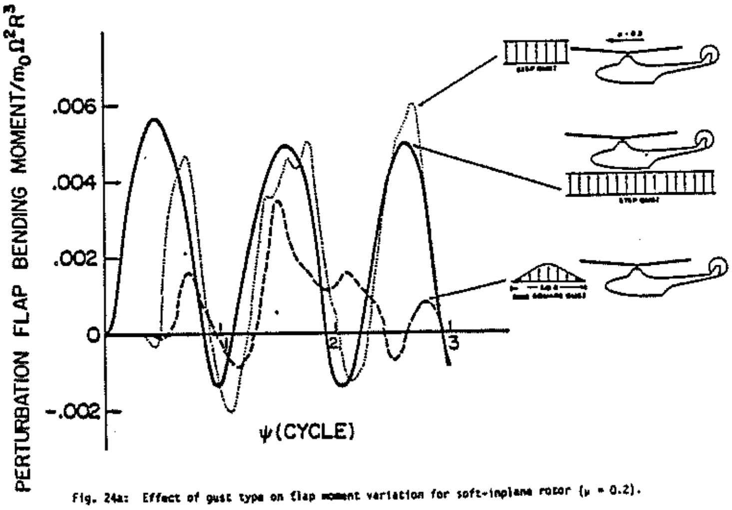

Fig. 24a: Effect of gust type on flap moment variation for soft-inplane rotor (μ = 0.2).

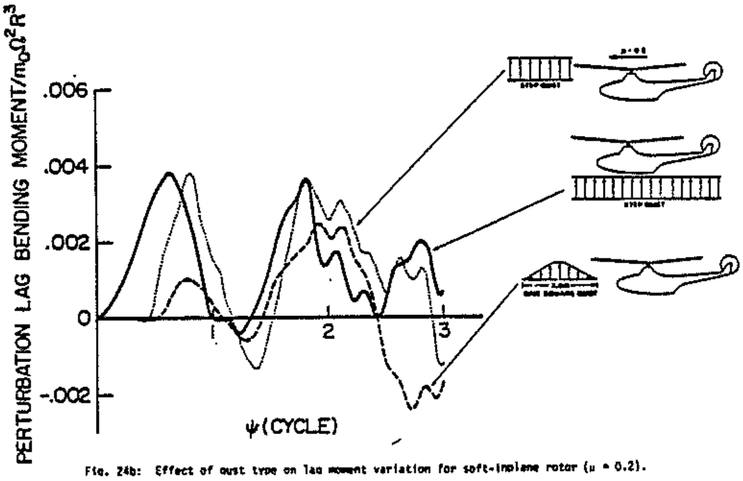

Fig. 24b: Effect of gust type on lag moment variation for soft-inplane rotor (μ = 0.2).

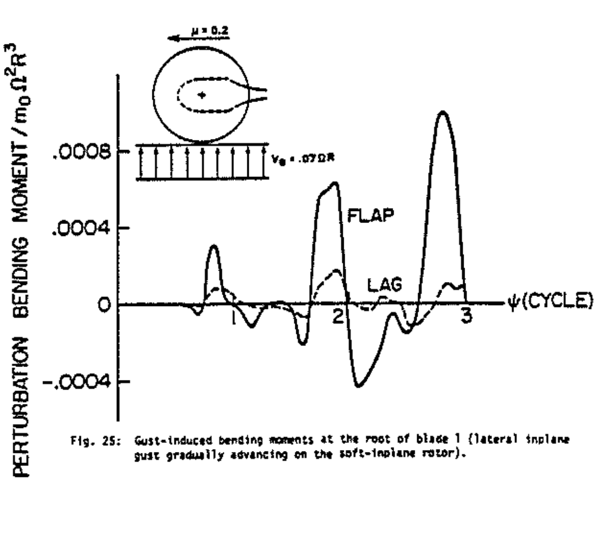

Fig. 25: Gust-induced bending moments at the root of blade 1 (lateral inplane gust gradually advancing on the soft-inplane rotor).

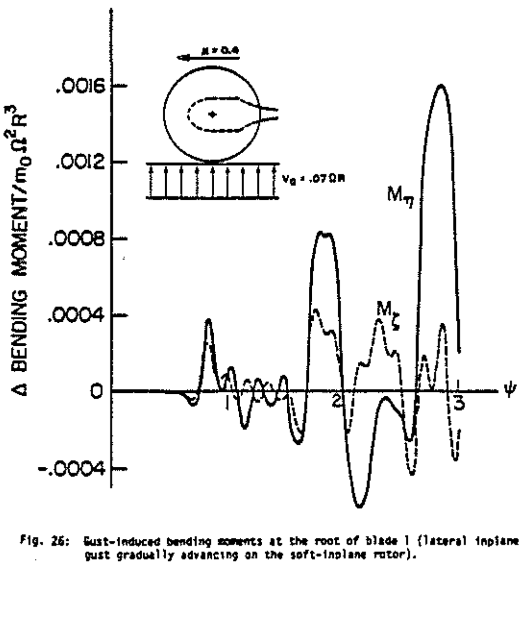

Fig. 26: Gust-induced bending moments at the root of blade 1 (lateral inplane gust gradually advancing on the soft-inplane rotor).